



Acceleration of continuous-time, high-cycle fatigue constrained problems in topology optimization

Shyam Suresh^{*}, Stefan B. Lindström, Carl-Johan Thore, Anders Klarbring

Division of Solid Mechanics, Department of Management and Engineering, Linköping University, SE-581 83 Linköping, Sweden

ARTICLE INFO

Keywords:

High-cycle fatigue
Extrapolation
Topology optimization
Endurance surface
Adjoint sensitivity analysis

ABSTRACT

An efficiency-enhanced procedure to treat continuous-time, high-cycle fatigue (HCF) constraints in topology optimization is presented. The HCF model predicts the evolution of fatigue damage at each point in the design domain using a system of ordinary differential equations. We employ gradient-based optimization and the fatigue sensitivities are determined using adjoint sensitivity analysis. As the predicted damage has history dependence, adjoint variables are solved via a stepwise backward procedure. Therefore, the computational cost increases in proportion to the number of time steps. To reduce this cost, we propose an extrapolation technique which is valid for all forms of periodic, proportional loads and most non-proportional loads and allows treatment of essentially an unlimited number of load cycles. Using this technique, several problems in both 2D and 3D are solved numerically where the objective is to minimize structural mass subjected to a fatigue constraint.

1. Introduction

In many industrial applications, fatigue due to both proportional and non-proportional loads threaten the life of components. High-cycle fatigue (HCF) is caused by small, predominantly elastic strains under a high number of load cycles ($\geq 10^3$ cycles). Thus, when designing mechanical components, we seek designs capable of withstanding such a load history. Introducing fatigue criteria in topology optimization (TO) formulations ensures that we get optimal designs protected from fatigue failure.

Examples of use of a fatigue constraint in TO are found in Holmberg et al. (2014) where it is implemented as a stress constraint, and in Jeong et al. (2018) and Collet et al. (2017), where cycle-counting algorithms are used. Another example is found in Oest and Lund (2017), where extensive load histories are solved with low computational cost. However, these models are restricted to proportional load histories and use rainflow counting algorithm. Additionally, Zhang et al. (2019) treats fatigue-life for non-proportional loads by using a signed von Mises stress at each point of the structure as a single stress measure. It also uses classical techniques, including rainflow counting, mean stress correction, and Palmgren–Miner's rule, initially developed for unidirectionally loaded structures. However, certain modes of stress reversal, including rotary stress states with constant principal stresses, give a constant signed von Mises stress, predicting zero fatigue damage. This

limitation constitutes a loop-hole that could potentially be exploited by the optimizer in case of non-proportional load.

In contrast to the above reviewed papers, we treat fatigue in TO by use of a continuous-time HCF model, developed in Ottosen et al. (2008). Such a HCF model was used in TO problems where both isotropic (Suresh et al., 2020), and transversely isotropic materials (Suresh et al., 2021) have been treated. The model is capable of handling arbitrary load histories, including non-proportional loads, without using a rainflow counting algorithm. However, due to high computational cost the method is presently only capable to TO problems involving a limited number of load cycles. To overcome this limitation, in this paper, we present an acceleration technique enabling treatment of essentially an unlimited number of load cycles provided that they consist of sequence repetitions.

In HCF models, neither geometry nor the material properties are affected by damage. Therefore, the stress evolution for a given load history is calculated in a separate initial step of the analysis. Then the so-obtained stresses are used for calculating the fatigue damage using a continuous-time fatigue model (Ottosen et al., 2008). This model uses ordinary differential equations that govern the time evolution of fatigue damage at each point in the design domain. Damage development only occurs when the stress state lies outside the evolving, so-called endurance surface.

^{*} Corresponding author.

E-mail addresses: shyam.suresh@liu.se (S. Suresh), stefan.lindstrom@liu.se (S.B. Lindström), carl-johan.thore@liu.se (C.-J. Thore), anders.klarbring@liu.se (A. Klarbring).

<https://doi.org/10.1016/j.euromechsol.2022.104723>

Received 8 March 2022; Received in revised form 14 June 2022; Accepted 24 June 2022

Available online 25 June 2022

0997-7538/© 2022 The Author(s). Published by Elsevier Masson SAS. This is an open access article under the CC BY license (<http://creativecommons.org/licenses/by/4.0/>).

Several modifications and extensions to the original continuous-time HCF model have been proposed. In [Ottosen et al. \(2018\)](#), the multiaxial fatigue criterion considers stress gradient effects, which crucially enables automatic handling of stress concentrations in complex geometries like holes and notches. Furthermore, in [Holopainen et al. \(2016\)](#), a continuous-time HCF model for transversely isotropic materials is formulated and in [Brighenti et al. \(2012\)](#), a more general expression for the endurance surface is developed, that demonstrates a fair agreement between modelled and experimentally-observed fatigue life for a range of steel alloys subjected to non-proportional stress. Additionally, the validity range and computational acceleration of the continuous-time HCF model are investigated in [Lindström et al. \(2020\)](#), and a modified version of the continuous-time HCF model is provided in [Lindström \(2020\)](#), that provides a better estimation of fatigue-damage for non-proportional loads.

In this paper, we use our previous work ([Suresh et al., 2020](#)), which is based on the original continuous-time fatigue model ([Ottosen et al., 2008](#)). The fatigue constraint in the TO problems is imposed on the maximum damage found in the design domain at the end of a given load history. The maximum operator is then approximated by means of an aggregation function, namely the p-norm ([Duysinx and Sigmund, 1998](#); [Yang and Chen, 1996](#); [Kennedy and Hicken, 2015](#)). Moreover, we use a gradient-based method for solving the TO problems, where the fatigue sensitivities are determined by the adjoint method. Since the predicted fatigue-damage is governed by an evolution problem, the fatigue sensitivities follow ([Suresh et al., 2020](#)) and the adjoint variables are solved via a backward, step-wise procedure. As a result, the computational time required to obtain the adjoint variables is quite high. Hence, an efficient procedure that speeds up the process is needed. In the present paper we show how this can be achieved by using extrapolation. The validity of such an extrapolation is based on the fact that it has been shown in [Lindström et al. \(2020\)](#) that the fatigue reaches steady-state condition for all forms of periodic proportional and most non-proportional loads.

2. Continuous-time fatigue model

In HCF, neither the geometry, nor the material properties are significantly influenced by damage until failure. Therefore the stress evolution $\sigma(t)$, $t \in [0, T]$, with T as the duration, is computed first from constitutive response and then these stresses are used to estimate the fatigue damage through the continuous-time HCF model suggested in [Ottosen et al. \(2008\)](#).

2.1. Overview

Following [Ottosen et al. \(2008\)](#), a moving endurance surface $\{\sigma | \beta(\sigma, \alpha) = 0\}$, with α as a back-stress tensor and β being the endurance function, is employed to define the fatigue model. The development of damage only occurs during loading, when the stress state also lies outside the endurance surface, i.e., $\beta > 0$ and $\dot{\beta} > 0$, where a superposed dot indicates time derivative. The endurance function is defined as

$$\beta(\sigma, \alpha) = \frac{1}{S_0} [\bar{\sigma} + A \text{tr}(\sigma) - S_0], \quad (1)$$

where $S_0 > 0$ and $A > 0$ are material parameters and $\text{tr}(\cdot)$ is the trace of the tensor. The effective stress $\bar{\sigma}$ is given as

$$\bar{\sigma} = \sqrt{\frac{3}{2} (s - \alpha) : (s - \alpha)},$$

where $s = \sigma - \frac{1}{3} \text{tr}(\sigma) \mathbf{I}$ is the deviatoric stress with \mathbf{I} as unit tensor and $:$ denotes Frobenius inner product.

The fatigue damage at a point is a scalar, real-valued function $D = D(t)$ that monotonously increases from $D = 0$ being no damage to $D = 1$ as critical failure. Following ([Suresh et al., 2020, 2021](#)), the state variables α and D are governed by a initial value problem:

$$\dot{\alpha} = C(s - \alpha)H(\beta)H(\dot{\beta}), \quad \alpha(0) = 0, \quad (2)$$

$$\dot{D} = K \exp(L\beta)H(\beta)H(\dot{\beta}), \quad D(0) = 0, \quad (3)$$

where $C > 0$, $K > 0$ and $L > 0$ are material parameters, and H is the Heaviside step function.

To obtain an explicit form for $\dot{\beta}$, we first take the time derivative of (1). Then with help of (2) and on rearranging we get

$$(S_0 + H(\beta)H(\dot{\beta})C\bar{\sigma})\dot{\beta} = \left[\frac{3}{2} \frac{(s - \alpha)}{\bar{\sigma}} + A \mathbf{I} \right] : \dot{\sigma}. \quad (4)$$

Whenever the right-hand side is positive, the fact that $S_0 + H(\beta)H(\dot{\beta})C\bar{\sigma} > 0$, (4) permits us to write $\dot{\beta}$ as a function:

$$\dot{\beta}(\sigma, \dot{\sigma}, \alpha) = \frac{1}{S_0 + H(\beta)C\bar{\sigma}} \left[\frac{3}{2} \frac{(s - \alpha)}{\bar{\sigma}} + A \mathbf{I} \right] : \dot{\sigma}. \quad (5)$$

Having the endurance function and its rate defined in (1) and (5), the fatigue damage is predicted by integrating the ODEs (2) and (3) for a given stress $\sigma = \sigma(t)$.

2.2. Time discretization

The fatigue problem is solved numerically. The time domain $[0, T]$ is discretized into a finite number of time steps of equal length Δt , i.e. $t_i = i\Delta t$, with $i = 0, 1, \dots, N$. The stress evaluations at different steps are denoted $\sigma_i = \sigma(i\Delta t)$, and $s_i = s(\sigma_i)$ while $\alpha_i = \alpha(i\Delta t)$ and $D_i = D(i\Delta t)$.

The increment of the endurance function in (5) is approximated as

$$\begin{aligned} \Delta\beta|_i &= \Delta t \dot{\beta} \left(\sigma_{i-1}, \frac{\sigma_i - \sigma_{i-1}}{\Delta t}, \alpha_{i-1} \right) \\ &= \frac{1}{S_0 + H(\beta|_{i-1})C\bar{\sigma}|_{i-1}} \left[\frac{3}{2} \frac{(s_{i-1} - \alpha_{i-1})}{\bar{\sigma}|_{i-1}} + A \mathbf{I} \right] : \Delta\sigma_i, \end{aligned} \quad (6)$$

with the stress increment $\Delta\sigma|_i = \sigma_i - \sigma_{i-1}$, and the effective stress $\bar{\sigma}|_i = \bar{\sigma}(\sigma_i, \alpha_i)$. The symbol $|_i$ denotes function evaluation at time step i . Expression (6) is only evaluated if the Frobenius inner product between the terms in the square parenthesis and the stress increment is positive, otherwise $\Delta\beta|_i = 0$.

The ODEs (2) and (3) are approximated by a forward Euler scheme as

$$\alpha_i - \alpha_{i-1} = C(s_{i-1} - \alpha_{i-1})H(\beta|_{i-1})\Delta\beta|_i, \quad (7)$$

$$D_i - D_{i-1} = K \exp(L\beta|_{i-1})H(\beta|_{i-1})\Delta\beta|_i. \quad (8)$$

3. Acceleration technique

In the continuous-time HCF model, integrating the full stress history across a large number of cycles often leads to a high computational cost. Furthermore, this cost increases even more when adjoint sensitivity analysis involving a spatially coupled terminal value problem is used. A key property of the HCF model is that when subjected to periodic, proportional and most non-proportional loads, there exists a steady-state condition such that the incremental damage per period approaches a constant value ([Lindström et al., 2020](#)). In such instances, an extrapolation technique can be used to accelerate the whole fatigue process.

3.1. Periodic, proportional stress history

For a periodic load with period τ , the integrated damage after time t is taken as $D(t)$. We take the incremental damage between periods as $\Delta D(t) = D(t) - D(t - \tau)$. If a steady-state exists, then $\lim_{t \rightarrow \infty} [D(t) - D(t - \tau)] \rightarrow \Delta D$, where ΔD is a fixed increment.

To demonstrate such a situation, we consider a 1D example. The fatigue model is numerically integrated for the 7050-T7451 aluminum alloy material. Using the fitted fatigue parameters, $S_0 = 113.3$ MPa, $A = 0.2611$, $C = 0.504$, $K = 5.11E - 6$ and $L = 2.556$, from [Lindström et al. \(2020\)](#), we integrate a uniaxial cyclic stress history on the form $\sigma(t) = \sigma_0 \sin(2\pi t/\tau) + \sigma_M$, where $\sigma_0 > 0$ is a constant stress amplitude and

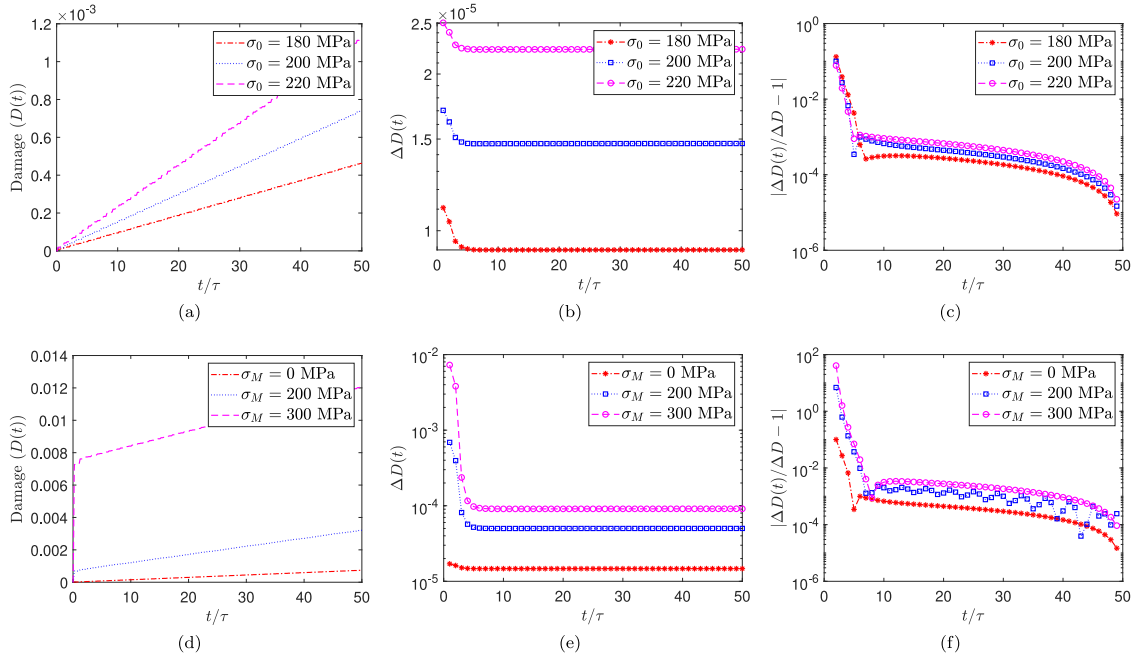


Fig. 1. Cyclic fatigue strength: (a) Damage development when $\sigma_M = 0$; (b) Incremental damage per period when $\sigma_M = 0$; (c) Development of relative difference to steady-state damage per period when $\sigma_M = 0$; (d) Damage development when $\sigma_0 = 200$ MPa; (e) Incremental damage per period when $\sigma_0 = 200$ MPa; and (f) Development of relative difference to steady-state damage per period when $\sigma_0 = 200$ MPa.

σ_M is the mean stress for a duration $T = 50\tau$ and $\Delta t = 0.001\tau$. Since the fatigue model is rate independent, the period τ is an arbitrary constant.

When $\sigma_M = 0$, the effective stress amplitude is the same as σ_0 and in Figs. 1(a–c), we provide the fatigue results for various stress amplitudes. The damage development for different stress amplitudes is similar to stair-case functions, see Fig. 1(a). The stair-case pattern arises due to the presence of the step function $H(\cdot)$ in (7) and (8). For the damage evolution, the corresponding damage increment per period is shown in Fig. 1(b), where after a certain period, the incremental damage achieves the steady-state condition. Furthermore, the magnitudes of relative difference between the incremental damage of subsequent steps are shown in Fig. 1(c). Considering a tolerance of 1%, the approximated steady-state incremental damage for a range stress amplitudes diminishes within 9 periods.

Similarly, for different mean stress values when $\sigma_0 = 200$ MPa, the fatigue results are shown in Figs. 1(d–f). The damage development for the corresponding mean stresses is shown in Fig. 1(d), while the incremental damage per period is shown in Fig. 1(e). We notice that the incremental damage achieves steady-state after a certain period for each of the mean stresses. It takes 6 periods for $\sigma_M = 0$ MPa, 9 periods for $\sigma_M = 200$ MPa and 10 periods for $\sigma_M = 300$ MPa to reach steady-state condition with tolerance of 1%. A key inference that is made here is that, as the mean stress value increases, the incremental damage takes a longer time to reach steady-state condition.

In the above example, we present the steady-state condition for the 1D example. However, it has been previously shown that for all periodic, proportional stress histories, the incremental damage per period tends to a steady-state condition, (Lindström et al., 2020).

3.2. Biaxial, non-proportional loading

In the previous section, using the continuous-time HCF model, we quantified the number of periods that it takes to achieve a steady-state condition for periodic, proportional load history. Now using this model, we do the same for non-proportional loads. As a demonstration, we take a biaxial, non-proportional loading.

Biaxial, non-proportional testing is often conducted on thin-walled cylinder specimens, subjected to elongation and torsion. Following

Lindström et al. (2020), we consider a combination of tension or compression and simple shear, fluctuating with zero mean stress, i.e.,

$$\begin{aligned}\sigma_{11} &= \frac{\sigma_0}{\sqrt{2} \cos(\frac{\Phi}{2})} \sin\left(2\pi \frac{t}{\tau}\right), \\ \sigma_{12} &= \frac{\sigma_0}{\sqrt{6} \cos(\frac{\Phi}{2})} \sin\left(2\pi \frac{t}{\tau} + \Phi\right),\end{aligned}\quad (9)$$

where Φ is a phase angle and $\sigma_{22} = \sigma_{33} = \sigma_{13} = \sigma_{23} = 0$. When $\Phi = 0$, then we have in-phase (IP) loading. Here the stress amplitude is σ_0 . The non-proportionality is introduced when $\Phi > 0$. This is called out-of-phase (OP) loading.

The fatigue damage for different phase angles are shown in Fig. 2. The damage development for the corresponding phase angles is shown in Fig. 2(a), while the incremental damage per period is shown in Fig. 2(b). We notice that the incremental damage achieves steady-state for $\Phi = 0^\circ$ and $\Phi = 60^\circ$ but not for $\Phi = 90^\circ$ (because the stress state is moving tangentially to the endurance surface (Lindström et al., 2020)). This is consistent with Lindström (2020), where steady-state and predictive capability for a wide range of non-proportional loads are demonstrated, with $\Phi = 90^\circ$ as the singular exception. Additionally, the magnitudes of relative difference between the incremental damage and the approximated steady-state is shown in Fig. 2(c). Considering a tolerance of 1%, the approximated steady-state incremental damage for $\Phi = 0^\circ$ and $\Phi = 60^\circ$ diminishes exponentially within 9 periods while for $\Phi = 90^\circ$ steady-state condition is never achieved.

3.3. Extrapolation

If steady-state occurs, the whole fatigue process can be significantly accelerated using extrapolation. Through extrapolation, we obtain the accumulated damage after $t_N \gg t_A > t_B = t_A - \tau$ as

$$D_N \approx \tilde{D}_N = D_{N_A} + \frac{t_N - t_A}{\tau} (D_{N_A} - D_{N_B}), \quad (10)$$

where $N_A = t_A/\Delta t$ and $N_B = t_B/\Delta t$.

We use the steady-state condition to estimate t_A , as shown in Algorithm 1. The algorithm makes use of a procedure CTF(N') which integrates the continuous-time HCF model for N' time steps, and

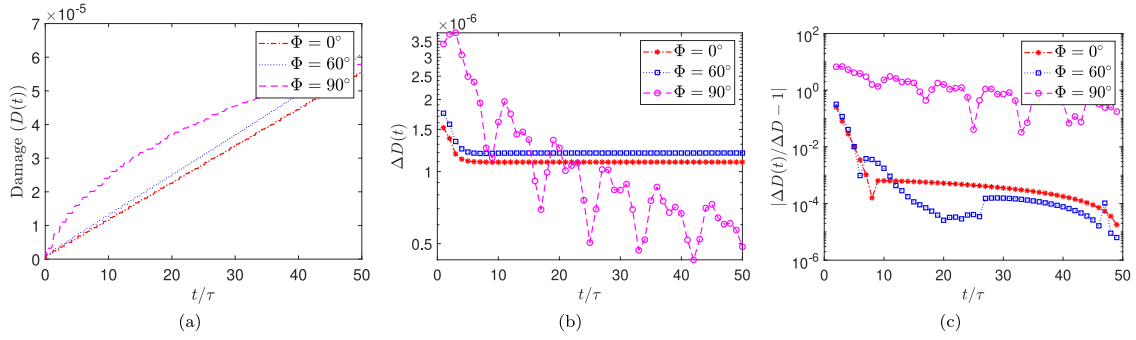


Fig. 2. Biaxial stress history when $\sigma_0 = 150$ MPa: (a) Damage development; (b) Incremental damage per period; and (c) Development of relative difference to steady-state damage per period.

returns the sequence $\{D_j\}_{j=0}^{N'}$ of the damage after each time step. A truncation sequence is employed in the algorithm to check whether the fatigue model has a steady-state condition for the time interval $[0, N'\Delta t]$. If the model does not exhibit a steady-state condition, then we increase the time domain by assigning $N' := 2N'$ to see if the model converges to a steady-state condition.

Algorithm 1 is utilized in fatigue constrained TO problems. In the FE model, using this algorithm, t_A is estimated for the element of maximum damage within the structure. With these values, the damage at all points is linearly extrapolated using (10). Furthermore, Algorithm 1 is utilized in the first iteration of the TO problem, and then t_A is fixed throughout the optimization procedure, and in the final iteration, the estimated t_A value is verified, i.e., the obtained value at the final iteration should be less than or equal to t_A .

Algorithm 1 Periodic, steady-state condition

```

1: procedure CALCULATE  $t_A$ 
2:   Inputs:  $N'$ ,  $\tau$ ,  $\Delta t$  and tol.
3:   % Integer time steps per period
4:    $k = \tau/\Delta t$ 
5:   % Set steady-state condition
6:    $SS = \text{False}$ 
7:   while not  $SS$  do
8:     % Get damage development
9:      $\{D_j\}_{j=0}^{N'} = \text{CTF}(N')$ 
10:    % Get approximate  $\Delta D$ 
11:     $\Delta D = D_{N'} - D_{N'-k}$ 
12:    % Get  $t_A$ 
13:     $j = 0$ 
14:    while  $j \leq N' - 2k$  and not  $SS$  do
15:       $j = j + k$ 
16:       $\Delta D_j = D_j - D_{j-k}$ 
17:       $SS = |\frac{\Delta D_j}{\Delta D} - 1| \leq \text{tol}$ 
18:       $t_A = j\Delta t$ 
19:    % Increase the duration
20:     $N' = 2N'$ 

```

4. Topology optimization problem formulation

We discretize the design domain Ω (Fig. 3) into n finite elements through the FE method. A standard density-based TO method is used, where the objective function is to minimize the total structural mass, i.e., the sum of elemental masses m_e scaled by the corresponding filter variable ρ_e , where $e = 1, 2, \dots, n$ is the element index. Through a design variable filter (Bruns and Tortorelli, 2001), these filtered variables ρ are connected to design variables \mathbf{x} . The design variable filter is used to avoid mesh dependency and checkerboard phenomena in the solution. The filtered variables $\rho(\mathbf{x})$ are called physical variables since they define the structural stiffness and the mass.

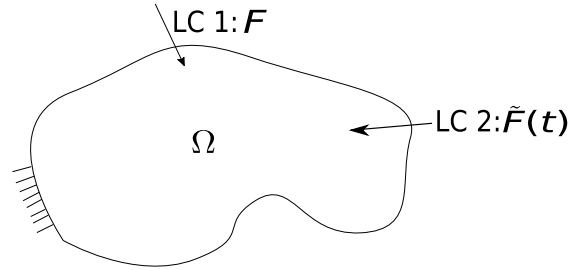


Fig. 3. Loading conditions with two load cases (LCs), where LC 1 contains a static load \mathbf{F} and LC 2 has a dynamic load history $\tilde{\mathbf{F}}(t)$.

The stiffness is penalized using the SIMP approach (Bendsoe and Sigmund, 2004; Christensen and Klarbring, 2009) to promote so-called black-and-white designs, i.e.,

$$\mathbf{K}(\rho(\mathbf{x})) = \sum_{e=1}^n (\rho_e(\mathbf{x}))^q \mathbf{K}_e, \quad (11)$$

where \mathbf{K}_e are elemental stiffness matrices and $q > 1$ is a penalization parameter.

Two load cases (LCs) are created to account for stiffness and fatigue, respectively, see Fig. 3. In the first LC we take a static load \mathbf{F} to compute the compliance (inverse of stiffness), while in the second LC a dynamic load history $\tilde{\mathbf{F}}(t)$ is used for calculating the fatigue-damage.

The equilibrium equation for the static load case reads

$$\mathbf{K}(\rho(\mathbf{x}))\mathbf{u} = \mathbf{F},$$

while for the fatigue LC, we assume quasi-static equilibrium, and consider a time-continuum of static problems as

$$\mathbf{K}(\rho(\mathbf{x}))\tilde{\mathbf{u}}(t) = \tilde{\mathbf{F}}(t), \quad \forall t \in [0, T].$$

In the above equilibrium equations, \mathbf{u} and $\tilde{\mathbf{u}}(t)$ are the displacement vectors for the corresponding load cases.

At each time step t_i , we have

$$\mathbf{K}(\rho(\mathbf{x}))\tilde{\mathbf{u}}_i = \tilde{\mathbf{F}}_i, \quad (12)$$

where $\tilde{\mathbf{F}}_i = \tilde{\mathbf{F}}(t_i)$, and the solution for a given design \mathbf{x} and time step i is denoted by $\tilde{\mathbf{u}}_i(\mathbf{x})$.

For a given $\tilde{\mathbf{u}}_i(\mathbf{x})$, the stress vector at a stress evaluation point inside an element e is computed as

$$\sigma_i(\mathbf{x}) = \sigma_i(\mathbf{x}, \tilde{\mathbf{u}}_i(\mathbf{x})) = \left(\frac{\rho_e(\mathbf{x}) - \epsilon}{1 - \epsilon} \right)^r \mathbf{E} \mathbf{B} \tilde{\mathbf{u}}_i(\mathbf{x}), \quad (13)$$

where \mathbf{E} is the constitutive tensor, and \mathbf{B} is the strain-displacement matrix. The parameter $r < q$ is introduced to avoid the stress singularity phenomenon (Bruggi, 2008; Holmberg et al., 2013), and $0 < \epsilon \ll 1$ is

the lower bound on the design variable. The above penalization factor gives exactly zero stress in void when $\rho_e = \epsilon$. Hence, no artificial damage is developed in such regions.

As mentioned, we perform a mass minimization of the component, where the total structural mass is minimized subject to fatigue constraints and a compliance constraint. The compliance is evaluated from the static load case as $\mathbf{F}^T \mathbf{u}(\mathbf{x})$. As for the fatigue load case, for a given load history $\bar{\mathbf{F}}$, the fatigue damage evaluated at a time step i in element e is $D_{i,e}(\mathbf{x})$. To ensure a minimum life for the body, we impose a damage constraint at the final time $T = t_N$,

$$\max_{e \in \{1,2,\dots,n\}} D_{N,e}(\mathbf{x}) \leq \bar{D}, \quad (14)$$

with $D_{N,e}(\mathbf{x})$ the accumulated damage in element e , and \bar{D} the maximum allowable damage anywhere in the structure. For a very large t_N , the practicality of evaluating the fatigue damage through continuous time fatigue model is compromised due to high computational cost. Therefore, the accumulated damage $D_{N,e} \approx \bar{D}_{N,e}$ in (14) is obtained via the extrapolation formula (10), leading, as shown in the numerical examples, to huge savings of computational time. Since the max-function in (14) is non-differentiable, we replace it with the p-norm (Kennedy and Hicken, 2015),

$$D^{PN}(\mathbf{x}) = \left[\sum_{e=1}^n (\bar{D}_{N,e}(\mathbf{x}))^P \right]^{\frac{1}{P}} \quad (15)$$

with $P > 1$ and D^{PN} as the approximated maximum damage. It holds that $D^{PN}(\mathbf{x}) \rightarrow \max_e D_{N,e}(\mathbf{x})$ when $P \rightarrow \infty$, but too large values for P can cause numerical difficulties.

Using (15), the mass minimization problem is now written as

$$(TO) \quad \begin{cases} \min_{\mathbf{x}} & \sum_{e=1}^n m_e \rho_e(\mathbf{x}) \\ \text{s.t.} & \begin{cases} D^{PN}(\mathbf{x}) \leq \bar{D}, \\ \mathbf{F}^T \mathbf{u}(\mathbf{x}) \leq \bar{C}, \\ \epsilon \leq x_e \leq 1, \quad e = 1, \dots, n_d, \\ x_e = \epsilon, \quad e = n_d + 1, \dots, n. \end{cases} \end{cases}$$

where n_d is the total number of elements that are considered in the design domain and \bar{C} is the maximum structural compliance. The compliance constraint is included to avoid all-void solutions, see the remark in Suresh et al. (2020).

In the above optimization problem, we have implemented the domain extension approach from Clausen and Andreassen (2017), where the external boundaries are treated in the same way as the internal boundaries. In this method, the optimization variables are prescribed to the lower limit ϵ in the extended parts. In (TO), we assume the last set of $n - n_d$ elements as the extended elements. The domain extension approach is used to get a smoother profile at the boundary and to avoid artificial structural reinforcement at the domain boundary.

5. Sensitivity analysis

We use adjoint sensitivity analysis for computational efficiency and, since the damage variables $D_{i,e}(\mathbf{x})$ has history dependence, the fatigue sensitivities derivation follow (Suresh et al., 2020).

5.1. Adjoint sensitivity formulation

The dynamic fields of the state variables are collected into a time sequence of vectors $\bar{\mathbf{u}}_i$ and \mathbf{v}_i . The state variable \mathbf{v}_i for each time step collects the back stress $\alpha_{i,e}$ in Voigt notation and damage $D_{i,e}$, i.e.

$$\mathbf{v}_i = [\mathbf{v}_{i,1}, \mathbf{v}_{i,2}, \dots, \mathbf{v}_{i,n}]^T, \quad i = 1, 2, \dots, N_A,$$

$$\mathbf{v}_{i,e} = \begin{bmatrix} \alpha_{i,e} \\ D_{i,e} \end{bmatrix}, \quad e = 1, 2, \dots, n.$$

For every i , the field variables $\bar{\mathbf{u}}_i$ and \mathbf{v}_i satisfy

$$\mathbf{R}(\mathbf{x})|_i = \mathbf{R}(\mathbf{x}, \bar{\mathbf{u}}_i(\mathbf{x})) = \mathbf{K}(\rho(\mathbf{x}))\bar{\mathbf{u}}_i(\mathbf{x}) - \bar{\mathbf{F}}_i = \mathbf{0}, \quad (16)$$

$$\mathbf{H}(\mathbf{x})|_i = \mathbf{H}(\mathbf{x}, \bar{\mathbf{u}}_i(\mathbf{x}), \bar{\mathbf{u}}_{i-1}(\mathbf{x}), \mathbf{v}_i(\mathbf{x}), \mathbf{v}_{i-1}(\mathbf{x})) = \mathbf{0}, \quad (17)$$

where $\mathbf{R}|_i$ and $\mathbf{H}|_i$ are the residuals for the equilibrium equation and evolution equations, respectively.

Recalling (7) and (8), we can write the residual in (17) as

$$\mathbf{H}(\mathbf{x})|_i = [\mathbf{H}(\mathbf{x})|_{i,1}, \mathbf{H}(\mathbf{x})|_{i,2}, \dots, \mathbf{H}(\mathbf{x})|_{i,m}]^T,$$

where $\mathbf{H}(\mathbf{x})|_{i,e}$ is the residual restricted to element e defined as

$$\mathbf{H}(\mathbf{x})|_{i,e} = \begin{bmatrix} \alpha_{i-1,e} + C(s_{i-1,e} - \alpha_{i-1,e})H(\beta|_{i-1})\Delta\beta|_{i,e} - \alpha_{i,e} \\ D_{i-1,e} + K\exp(L\beta|_{i-1,e})H(\beta|_{i-1})\Delta\beta|_{i,e} - D_{i,e} \end{bmatrix}. \quad (18)$$

We multiply by arbitrary vectors λ_i and γ_i to (16) and (17) and obtain the following augmented version of (15):

$$\hat{D}^{PN}(\mathbf{x}) = \left[\sum_{e=1}^n (\bar{D}_{N,e}(\mathbf{x}))^P \right]^{\frac{1}{P}} - \sum_{i=1}^{N_A} \lambda_i^T \mathbf{R}(\mathbf{x})|_i - \sum_{i=1}^{N_A} \gamma_i^T \mathbf{H}(\mathbf{x})|_i \quad (19)$$

Taking the derivative of (19) with respect to x_j , we get

$$\begin{aligned} \frac{d\hat{D}^{PN}(\mathbf{x})}{dx_j} &= \frac{1}{P} \left[\sum_{e=1}^n (\bar{D}_{N,e}(\mathbf{x}))^P \right]^{\frac{1}{P}-1} \left[\sum_{e=1}^n P \bar{D}_{N,e}^{P-1} \frac{d\bar{D}_{N,e}(\mathbf{x})}{dx_j} \right] \\ &\quad - \sum_{i=1}^{N_A} \lambda_i^T \left[\partial_1 \mathbf{R}|_i + \partial_2 \mathbf{R}|_i \frac{d\bar{\mathbf{u}}_i}{dx_j} \right] \\ &\quad - \sum_{i=1}^{N_A} \gamma_i^T \left[\partial_1 \mathbf{H}|_i + \partial_2 \mathbf{H}|_i \frac{d\bar{\mathbf{u}}_i}{dx_j} + \partial_3 \mathbf{H}|_i \frac{d\bar{\mathbf{u}}_{i-1}}{dx_j} \right. \\ &\quad \left. + \partial_4 \mathbf{H}|_i \frac{d\mathbf{v}_i}{dx_j} + \partial_5 \mathbf{H}|_i \frac{d\mathbf{v}_{i-1}}{dx_j} \right], \end{aligned} \quad (20)$$

where ∂_a denotes differentiation with respect to the a th argument and the derivative $d\bar{D}_{N,e}(\mathbf{x})/dx_j$ is calculated using (10), which is

$$\frac{d\bar{D}_{N,e}(\mathbf{x})}{dx_j} = \frac{dD_{N_A,e}(\mathbf{x})}{dx_j} + \frac{t_N - t_A}{\tau} \left[\frac{dD_{N_A,e}(\mathbf{x})}{dx_j} - \frac{dD_{N_B,e}(\mathbf{x})}{dx_j} \right]. \quad (21)$$

Substituting (21) in (20), writing $D_{N_A,e} = \mathbf{e}_e^T \mathbf{v}_{N_A}$ and $D_{N_B,e} = \mathbf{e}_e^T \mathbf{v}_{N_B}$, with \mathbf{e}_e as a column vector that contains only zeros except for a one in the position corresponding to $D_{N_A,e}$ and $D_{N_B,e}$, respectively and then rearranging the terms in (20), we get:

$$\begin{aligned} \frac{d\hat{D}^{PN}(\mathbf{x})}{dx_j} &= - \sum_{i=1}^{N_A} \lambda_i^T \mathbf{R}(\mathbf{x})|_i - \sum_{i=1}^{N_A} \gamma_i^T \mathbf{H}(\mathbf{x})|_i \\ &\quad - \left[\lambda_{N_A}^T \partial_2 \mathbf{R}|_{N_A} + \gamma_{N_A}^T \partial_2 \mathbf{H}|_{N_A} \right] \frac{d\bar{\mathbf{u}}_{N_A}}{dx_j} - \left[\gamma_{N_A}^T \partial_4 \mathbf{H}|_{N_A} \right] \frac{d\mathbf{v}_{N_A}}{dx_j} \\ &\quad - \left(1 + \frac{t_N - t_A}{\tau} \right) (D^{PN})^{1-P} \left(\sum_{e=1}^n \bar{D}_{N,e}^{P-1} \mathbf{e}_e^T \right) \frac{d\mathbf{v}_{N_A}}{dx_j} \\ &\quad - \left(\frac{t_N - t_A}{\tau} \right) (D^{PN})^{1-P} \left(\sum_{e=1}^n \bar{D}_{N,e}^{P-1} \mathbf{e}_e^T \right) \frac{d\mathbf{v}_{N_B}}{dx_j} \\ &\quad - \sum_{i=2}^{N_A} \left[\lambda_{i-1}^T \partial_2 \mathbf{R}|_{i-1} + \gamma_{i-1}^T \partial_2 \mathbf{H}|_{i-1} + \gamma_i^T \partial_3 \mathbf{H}|_i \right] \frac{d\bar{\mathbf{u}}_{i-1}}{dx_j} \\ &\quad - \sum_{i=2}^{N_A} \left[\gamma_{i-1}^T \partial_4 \mathbf{H}|_{i-1} + \gamma_i^T \partial_5 \mathbf{H}|_i \right] \frac{d\mathbf{v}_{i-1}}{dx_j}. \end{aligned}$$

The adjoint variables, λ_i and γ_i , are now required to satisfy following discrete terminal value problem:

$$\begin{bmatrix} \mathbf{K}(\mathbf{x}) & \left(\partial_2 \mathbf{H} \Big|_{N_A} \right)^T \\ \mathbf{0} & -\mathbf{I} \end{bmatrix} \begin{bmatrix} \lambda_{N_A} \\ \gamma_{N_A} \end{bmatrix} = \begin{bmatrix} \mathbf{0} \\ \left(1 + \frac{t_{N-t_A}}{\tau} \right) (D^{PN})^{1-P} \left(\sum_{e=1}^n \bar{D}_{N,e}^{P-1} \mathbf{e}_e^T \right) \end{bmatrix} \quad (22)$$

$$\begin{bmatrix} \mathbf{K}(\mathbf{x}) & \left(\partial_2 \mathbf{H} \Big|_{i-1} \right)^T \\ \mathbf{0} & -\mathbf{I} \end{bmatrix} \begin{bmatrix} \lambda_{i-1} \\ \gamma_{i-1} \end{bmatrix} = - \begin{bmatrix} \left(\partial_3 \mathbf{H} \Big|_i \right)^T \\ \left(\partial_5 \mathbf{H} \Big|_i \right)^T \gamma_i - \left[\left(\frac{t_{N-t_A}}{\tau} \right) (D^{PN})^{1-P} \left(\sum_{e=1}^n \bar{D}_{N,e}^{P-1} \mathbf{e}_e^T \right) \delta_{iN_B} \right] \end{bmatrix}, \quad (23)$$

which is solved backwards for $i = N_A, N_A - 1, \dots, 2$. Here δ_{ij} is the Kronecker delta. The final sensitivity expression becomes

$$\frac{d \hat{D}^{PN}(\mathbf{x})}{dx_j} = - \sum_{i=1}^{N_A} \lambda_i^T \frac{\partial \mathbf{R}(\mathbf{x})}{\partial x_j} \Big|_i - \sum_{i=1}^{N_A} \gamma_i^T \frac{\partial \mathbf{H}(\mathbf{x})}{\partial x_j} \Big|_i. \quad (24)$$

The original sensitivity formulation shown in Suresh et al. (2020) emerges as a special case when $t_A = t_N$, i.e., $N_A = N$. This happens when the HCF model does not exhibit steady-state condition.

5.2. Solving the adjoint system

For additional computational efficiency, we exploit the structure of the coefficient matrices in the adjoint Eqs. (22) and (23). Considering (23) and $t_A = t_N$, we first solve γ_{i-1} and then λ_{i-1} as follows:

$$-\gamma_{i-1} = -(\partial_5 \mathbf{H} \Big|_{i-1})^T \gamma_i, \quad (25)$$

$$\mathbf{K}(\mathbf{x}) \lambda_{i-1} = -(\partial_3 \mathbf{H} \Big|_{i-1})^T \gamma_i - (\partial_2 \mathbf{H} \Big|_{i-1})^T \gamma_{i-1}. \quad (26)$$

We note that when using a direct linear solver, $\mathbf{K} \in \mathbb{R}^{m \times m}$ need only be factorized once for each design. Since the (Cholesky) factorization is needed anyway to solve the state problem, the cost for solving (26) is mainly that of solving two triangular systems, i.e. around $2n^2$ floating-point operations per time step (probably less than n^2 due to sparsity). However, the cost of factorization is $> n^2$ and will eventually dominate unless one considers very long repetition sequences of the load.

As for (25) the cost for solving it is negligible. The computational cost in the sensitivity analysis is thus dominated by the solving of (26).

While the savings of computational time is completely dominated by the use of the extrapolation, the cost for the sensitivity analysis in the thereby obtained TO problem is still not negligible. Therefore, the next section presents a way to speed up the sensitivity analysis further, similarly to elastoplasticity (Wang et al., 2017).

5.3. Simplification of sensitivity analysis

To obtain λ_i and γ_i at each time step, we require solutions to N_A linear systems. Hence, the total computational cost is roughly proportional to the number of time steps.

In the continuous-time HCF model, we can distinguish two types of time steps: non-fatigue steps (no damage within the structure), i.e. when stress-state at all points in the design domain lies within the endurance surface ($\beta < 0$) or in unloading condition ($\dot{\beta} < 0$), and fatigue steps (damage development anywhere within the structure). Based on these observations, we find that the non-fatigue time steps can be identified and eliminated from the sensitivity analysis.

In the non-fatigue step, $i - 1$, we have $H(\beta) \Big|_{i-1} = 0$. The elemental residual $\mathbf{H}(\mathbf{x}) \Big|_{i,e}$ in (18), then becomes

$$\mathbf{H}(\mathbf{x}) \Big|_{i,e} = \begin{bmatrix} \alpha_{i-1,e} - \alpha_{i,e} \\ D_{i-1,e} - D_{i,e} \end{bmatrix}. \quad (27)$$

Using (27), the partial derivatives in (25) and (26) are

$$\partial_2 \mathbf{H} \Big|_{i-1} = \mathbf{0}, \quad \partial_3 \mathbf{H} \Big|_{i-1} = \mathbf{0}, \quad \partial_5 \mathbf{H} \Big|_{i-1} = \mathbf{I}. \quad (28)$$

Substituting (28) into (25) and (26), we get $\gamma_{i-1} = \gamma_i$ and $\lambda_{i-1} = \mathbf{0}$. With the obtained adjoint variables and derivative $\partial_1 \mathbf{H}(\mathbf{x})$ at time step $i - 1$ in (24) becomes $\partial_1 \mathbf{H}(\mathbf{x}) \Big|_{i-1} = \mathbf{0}$ from (27), and the sensitivity value obtained for $i - 1$ becomes zero. Thus, time step $i - 1$ can be skipped from the sensitivity analysis without loss of accuracy.

6. Numerical examples

The proposed method is implemented in the in-house FE program TRINITAS, (Torstenfelt, 2012). The optimization problem (TO) is solved by using the Method of Moving Asymptotes (MMA), (Svanberg (1987), on a desktop computer with an Intel(R) Core(TM) i9-10980XE CPU @ 3.00 GHz with 18 cores. The increase and decrease factors for the asymptotes have been reduced to 1.05 and 0.65, respectively.

Using 7050-T7451 aluminum alloy, several examples, particularly a 2D L-shaped beam, discretized by bi-linear quadrilateral plane stress FEs having thickness 1 mm, and a 3D bracket, discretized by 6-noded solid wedge elements and 8-noded solid brick elements, are tested. For the concerned material, the Young modulus is 70 GPa, the density is 2700 kg/m³, and the Poisson ratio is 0.33. We take the values of the penalization parameters as $q = 3$ and $r = 0.5$. The initial design variables are taken as $x_e = 0.75$ and the lower bound on the design variables is $\epsilon = 0.001$. The problems are solved with the density filter radii as 0.6 mm for 2D examples and 2.3 mm for the 3D example, and the exponent of the p-norm $P = 8$. The stresses σ_i obtained for the fatigue load case is calculated using (13).

The maximum structural compliance \bar{C} in (TO) is determined by performing a compliance minimization subjected to a mass constraint without fatigue constraint. The optimization problem is solved for 30% of the original structural mass and the compliance obtained is set as \bar{C} . The maximum fatigue damage \bar{D} in (TO) is selected such that we try to obtain an infinite life in the structure. At infinite-life, we expect that the endurance surface is moved to a position where the whole stress cycle is inside it. From Ottosen et al. (2008), Holopainen et al. (2016) and Lindström et al. (2020), it is found that the damage per period for getting an infinite life is around $1E-7$. Hence, for the presented examples, the maximum fatigue damage \bar{D} is selected close to that value.

6.1. Computational time

We evaluate the computational time for the plate-with-hole geometry, shown in Fig. 4. The dimensions of the model are $L_0 = 100$ mm and $R = 0.4L_0$ and the geometry has a thickness of 10 mm. Using symmetry, only a quarter of the geometry is modelled using 6000 3D 8-node brick elements. At the left and bottom faces, symmetry boundary conditions are applied. A uniformly-distributed load $Q_0 = 50$ MPa is applied to the right face as a static load case, while a uniformly-distributed, periodic load $\bar{Q}(t) = Q_0 \sin(2\pi t/\tau)$ is used for the dynamic load case, where $T = 20\tau$, $\tau = 1$, $\Delta t = 0.01\tau$, and $N' = T/\Delta t$.

The optimization problem (TO) is solved for 5 MMA iterations, for which the computational time is evaluated. Breakdown of timings, i.e., fatigue analysis, sensitivity analysis and total (fatigue + sensitivity analyses) for the considered geometry is shown in Fig. 5.

Using the conventional approach, i.e. the stress history is fully integrated to $t_N = 20\tau$ (red bar), from the figure, it is evident that the major computational time is spent on sensitivity analysis, and therein on the solution of the adjoint variables.

The dotted red bars show the projected computational time that it takes to solve the TO problem when subjected to a long load history, $t_N = 1E5\tau$. Here, we can clearly see that it is practically impossible to solve fatigue TO problems for structures subjected to long load

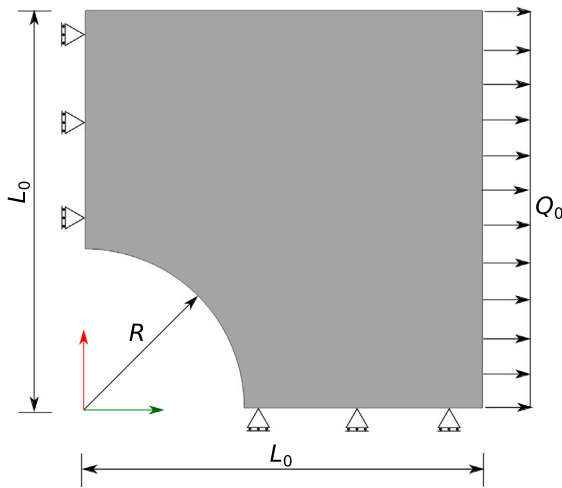


Fig. 4. Plate-with-hole geometry.

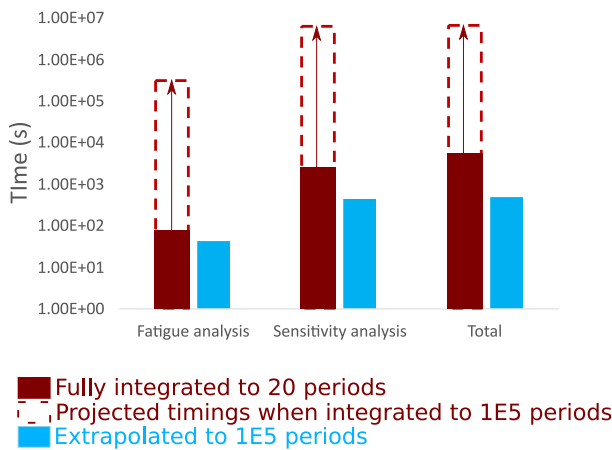


Fig. 5. Computational time calculation.

histories by integrating the entire loading history. Hence, we employ the extrapolation technique.

For the considered geometry, using Algorithm 1, the steady-state condition exist after $t_A = 12\tau$. Therefore, we fully integrate the fatigue model until t_A with extrapolation to $t_N = 1E5\tau$ (blue bar). In this case timings for fatigue and sensitivity analyses are improved considerably by a factor of around $1E5$. Through extrapolation, we are thus capable of solving TO problems for structures subjected to long load histories.

6.2. L-shaped beam with a cyclic, proportional load history

For the first example, we consider an L-shaped beam, where the dimensions used for this geometry are shown in Fig. 6, with $L_1 = 100$ mm. The design domain is discretized by 57600 elements. The top edge of the beam is clamped. Two load cases are created, where the first load case is a static load $Q_1 = 200$ N for compliance evaluation, while the second load case takes the periodic load history, $\bar{Q}_1(t) = Q_1 \sin(2\pi t/\tau)$, with $T = 20\tau$, $\tau = 1$, $\Delta t = 0.01\tau$, and $N' = T/\Delta t$, for fatigue estimation. The grey regions in Fig. 6 indicate elements domain extension approach, and the black region under the load indicates elements that are not included in optimization.

The optimization problem (TO) is solved for three cases. In the first case, the fatigue model is fully integrated to a time $t_N = 20\tau$ with fatigue bound $\bar{D} = 1E-5$, while in the second and third case, we use Algorithm 1 to identify the steady-state condition and for the

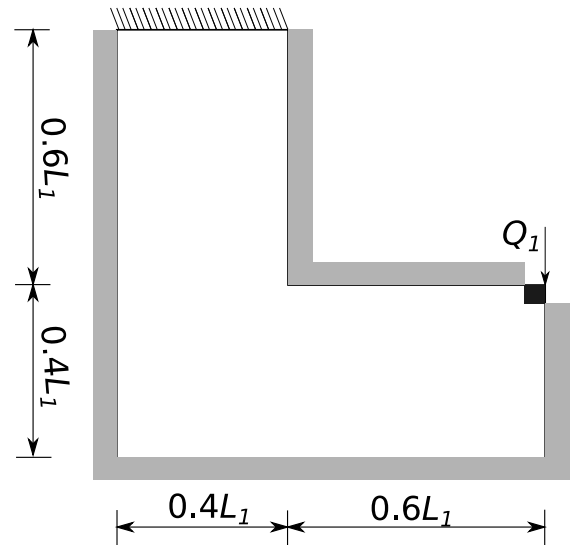


Fig. 6. Geometry of the L-shaped beam domain.

considered example, the steady-state exists after $t_A = 13\tau$. Thus, the fatigue model is integrated until t_A with extrapolation to $t_N = 20\tau$ and $t_N = 20E5\tau$, respectively. The fatigue bound for the second case is taken same as first case, i.e., $\bar{D} = 1E-5$. For the third case, we take the fatigue bound as $\bar{D} = 0.9$ to make the target damage per period comparable to the first two cases. The compliance bounds for all cases are taken as $\bar{C} = 0.21$ Nmm.

Table 1 provides optimized results of the L-shaped beam for three cases. In the first row, the profiles of the optimized model for the three cases are provided, while in second row, we see the corresponding fatigue-damage distribution within the structure. In the first column, the optimized model of the L-shaped beam after 1000 MMA iterations is shown when the stress history is fully integrated. The computational time required to solve this case is around 6 h. We notice that in the optimized model, there is a smooth radius at the re-entrant edge, thereby reducing high stress concentrations and thus prolonging the life of the structure.

In the second column, the optimized model of the L-shaped beam is shown for the second case. Here the same problem as in first case is solved with extrapolation. We notice that the profile obtained with extrapolation is roughly similar to the optimized model with full integration (first column). The computational time required to solve this case is around 3 h after 1000 iterations. The third column gives the optimization result when extrapolated to $t_N = 20E5\tau$. In this case, the maximum fatigue-damage within the optimized structure is found to less than critical failure, i.e., $D < 1$. The computational time taken here is exactly same as for the second case, i.e., around 3 h. Fatigue damage is much more localized to the surface in the high-cycle case (third column, Table 1). This is because transient effects become negligible.

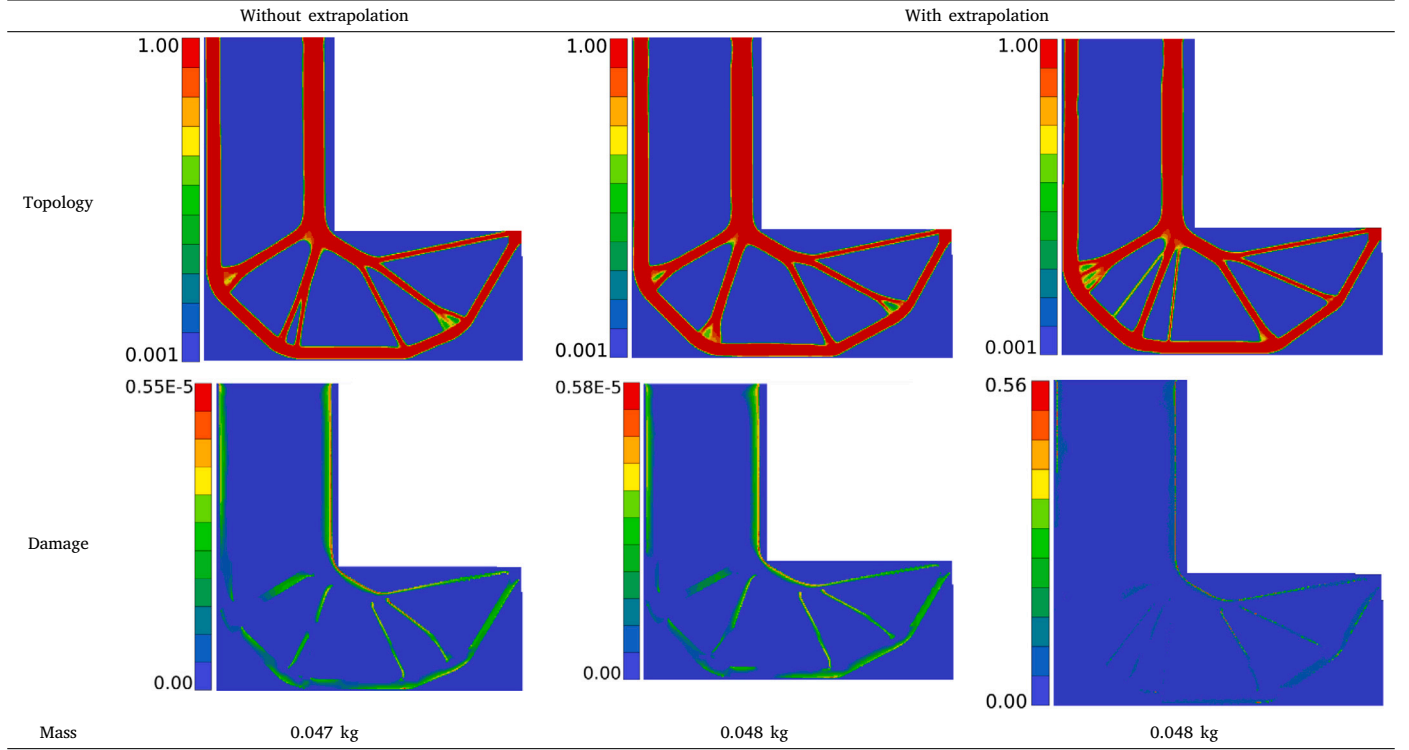
6.3. L-shaped beam with repeats in loading spectrum, proportional load history

We again use the L-shaped beam from Fig. 6. However, for the fatigue load case, the loading spectrum shown in Fig. 7 is taken, with load history as $\bar{Q}_1(t) = Q_1 S_f(t)$. Here $S_f(t)$ is a pseudo-random function, which is a linear interpolation between 20 normally randomized values at $\tau/20$ interspersing when $t \in [0, \tau]$. This sequence is repeated, $S_f(t + \tau) = S_f(t)$, with period $\tau = 20$ (Fig. 7), and we use $\Delta t = 0.0025\tau$, $T = 5\tau$ and $N' = T/\Delta t$.

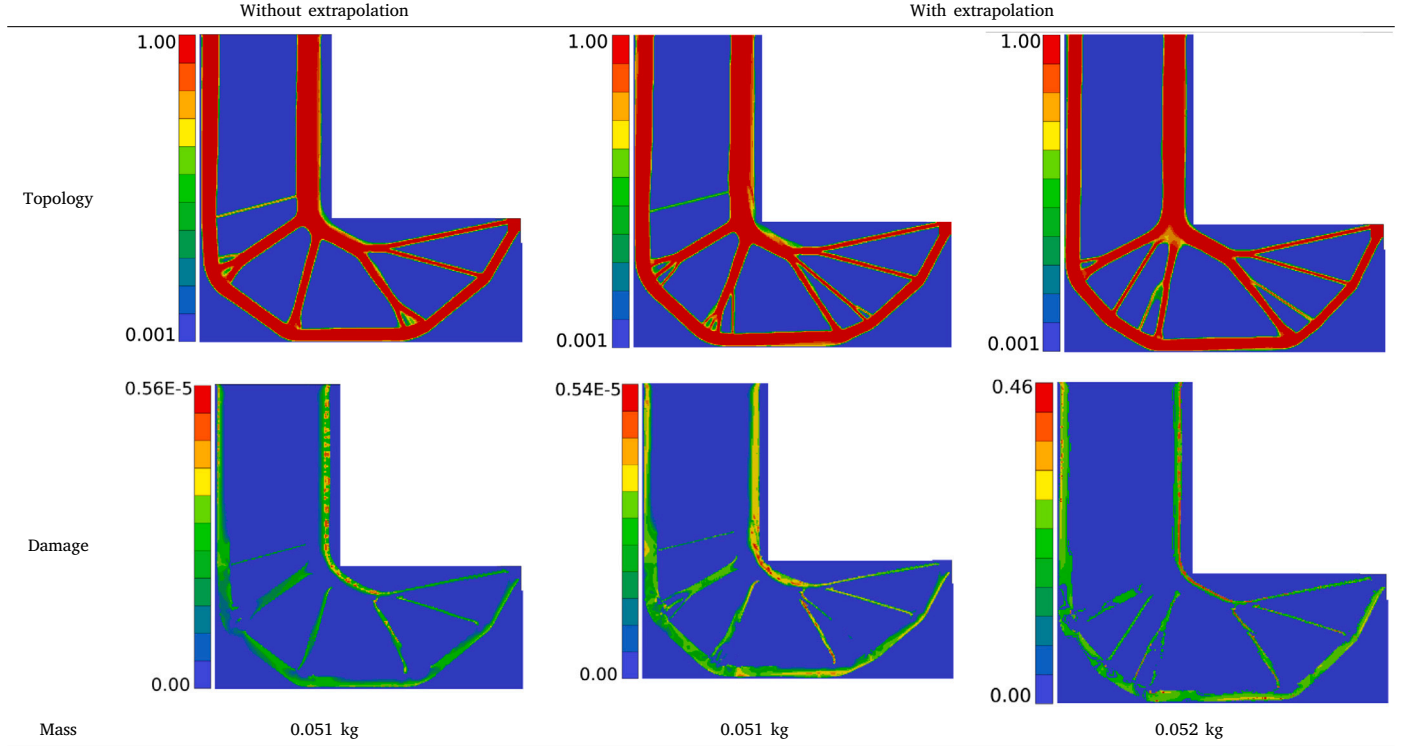
Similar to the first example, we solve the (TO) problem for three cases. In the first case, the fatigue model is fully integrated to a time of

Table 1

Optimized results of the L-shaped beam when subjected to a cyclic load history; (a) Fully integrated to a time period of $t_N = 20\tau$ without extrapolation; (b) Extrapolated to $t_N = 20\tau$; (c) Extrapolated to $t_N = 20E5\tau$.

**Table 2**

Optimized results of the L-shaped beam when subjected to repeats in loading spectrum; (a) Fully integrated to $t_N = 5\tau$; (b) Extrapolated to $t_N = 5\tau$; (c) Extrapolated to $t_N = 5E5\tau$.



$t_N = 5\tau$ with $\bar{D} = 1E - 5$, while in the second case, using extrapolation (10), the fatigue damage is extrapolated to $t_N = 5\tau$ with the above fatigue bound. For the considered example, steady-state exists after $t_A = 4\tau$, and thus the fatigue model is integrated until t_A with extrapolation. In the third case, the fatigue model is extrapolated to $t_N = 5E5\tau$ with

fatigue bound as $\bar{D} = 0.9$. Like the previous example, the maximum fatigue-damage within the structure before optimization is found to be greater than 1, which is more than critical failure value ($D = 1$). Hence we chose the above fatigue bound. The compliance bounds for all cases are taken as $\bar{C} = 0.21$ Nmm.

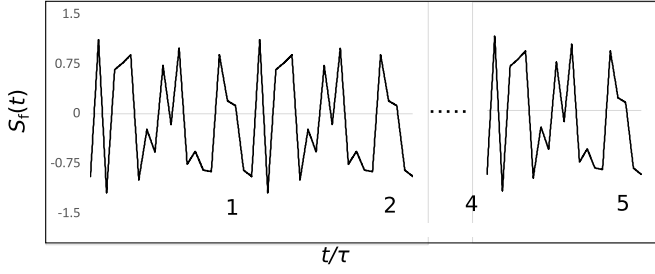


Fig. 7. Repeats in loading spectrum.

Table 2 provides optimized results of the L-shaped beam for three cases. The profiles of the optimized model for the three cases are provided in the first row, while the second row gives the corresponding fatigue-damage distribution within the structure. In the first column, the optimized model of the L-shaped beam is shown when the stress history is fully integrated. The computational time required to solve this case is around 8 h.

In the second column, the optimized model of the L-shaped beam is shown for the second case. Here the same problem as in first case is solved with extrapolation. We note that there is a slight difference in topologies of the optimized model in the first and second cases. The reason for the change in profiles is probably due to the non-convexity of the problem (local optima). However, we obtain similar structural mass. The computational time required to solve this case is around 5 h. For the third case, the optimization result is shown in the final column when the fatigue model is extrapolated to $t_N = 5E5\tau$ and the computational time taken here is same as the second case, i.e., around 5 h.

Table 3

Optimized results of the L-shaped beam when subjected to biaxial, non-proportional loads; (a) Fully integrated to $t_N = 20\tau$; (b) Extrapolated to $t_N = 20\tau$; (c) Extrapolated to $t_N = 5E5\tau$.

	Without extrapolation	With extrapolation	
Topology			
Damage			
Mass	0.068 kg	0.069 kg	0.079 kg

6.4. L-shaped beam with biaxial, non-proportional load history

We use the L-shaped beam from Fig. 6 with the loading condition shown in Fig. 8. Three load cases are created, where the first and second load cases consist of static loads $Q_{2y} = 200\text{ N}$ and $Q_{2x} = 300\text{ N}$ for compliance evaluations, while the third load case takes a biaxial load history, $\tilde{Q}_{2y}(t) = Q_{2y} \sin(2\pi t/\tau)$, and $\tilde{Q}_{2x}(t) = Q_{2x} \sin(2\pi t/\tau - \Phi)$ with $T = 20\tau$, $\Phi = 45^\circ$, $\tau = 1$, $\Delta t = 0.025\tau$, and $N' = T/\Delta t$, for fatigue estimation.

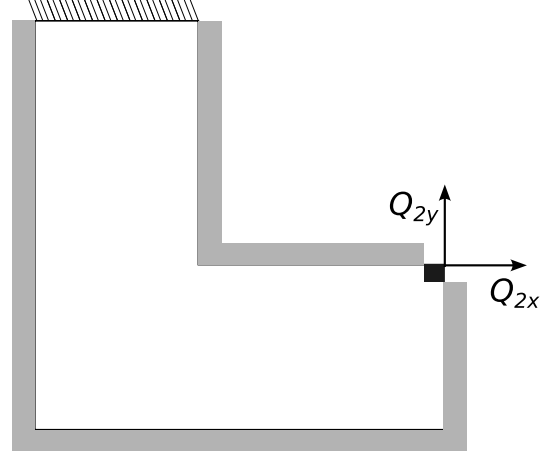


Fig. 8. Biaxial loading condition.

We solve the optimization problem (T0) for three cases. In the first case, we fully integrate the fatigue model to a time $t_N = 20\tau$ with fatigue bound $\bar{D} = 5E-5$, while in the second and third case, we use Algorithm 1 to identify the steady-state condition. For the considered example, the steady-state exists after $t_A = 11\tau$. Thus, the fatigue model is integrated until t_A with extrapolation to $t_N = 20\tau$ and $t_N = 4E5\tau$, respectively. The fatigue bound for the second case is taken same as

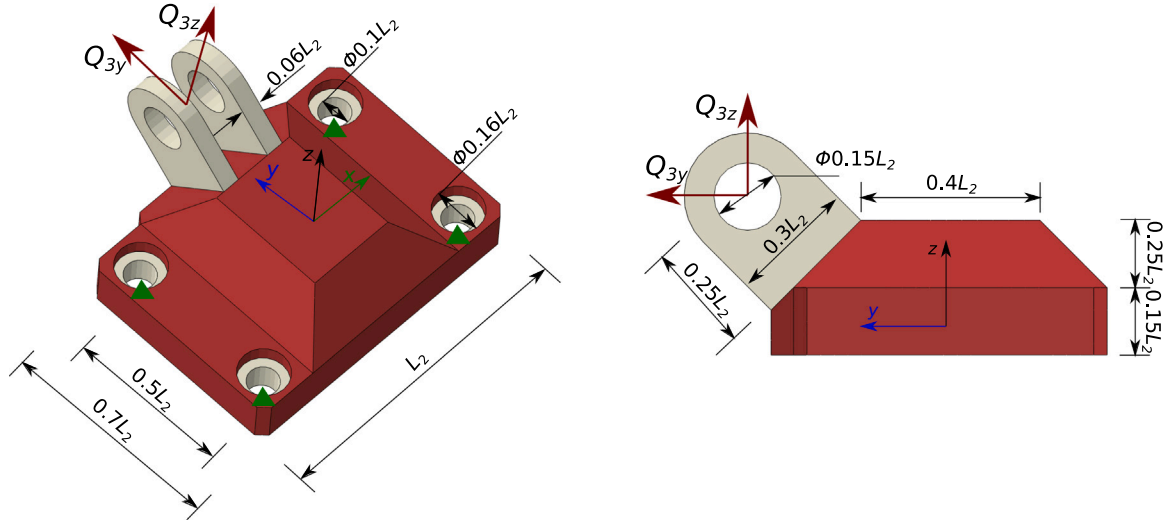


Fig. 9. Geometry of the 3D bracket.

first case and for the third case, we take the fatigue bound as $\bar{D} = 0.9$. For all cases, the compliance bound for each static load cases is taken as $\bar{C} = 0.25 \text{ Nmm}$.

Table 3 provides optimization results of the L-shaped beam with biaxial loading for three cases. The profiles of the optimized model for the three cases are provided in the first row, while the second row gives the corresponding fatigue-damage distribution within the structure. In the first column, the optimized model of the L-shaped beam is shown when the stress history is fully integrated. The static loads Q_{2y} and Q_{2x} induce a high bending moment in the region close to the clamped edge. Therefore, on optimization, fatigue damage starts to dominate at the vertical boundaries near the clamped edge due to high bending stresses. As a result more material is distributed near the clamped regions. The computational time required to solve this case after 1000 MMA iterations is around 12 h.

The second column provides the optimized model of the L-shaped beam for the second case, where the same problem as in first case is solved with extrapolation. Due to the non-convexity of the problem, there is a difference in topologies of the optimized model in the first and second cases. However, we obtain similar structural mass. The computational time required to solve this case is around 6 h. For the third case, the optimization result is shown in the final column when the fatigue model is extrapolated to $t_N = 4E5\tau$ and the computational time taken here is same as the second case.

As mentioned in Section 3, it is possible to achieve steady-state for most non-proportional loads. However, for the considered example, for phase angles $\Phi > 70^\circ$, the fatigue model does not achieve steady-state condition.

6.5. 3D bracket with periodic load history

For the final example, we take a 3D bracket shown in Fig. 9. The dimensions of the geometry is shown in Fig. 9 with $L_2 = 100 \text{ mm}$. The model is discretized by 73216 3D elements (5056 6-noded solid wedge elements + 68160 8-noded solid brick elements) and at 4 bolt locations, we have fixed boundary conditions. Like the previous example, two load cases are created, where the first load case is a static load in the form of surface load $Q_{3y} = Q_{3z} = 3.5E7 \text{ N/mm}^2$ for compliance evaluation, while the second load case takes the periodic load history, $\bar{Q}_{3y}(t) = Q_{3y} \sin(2\pi t/\tau)$ and $\bar{Q}_{3z}(t) = Q_{3z} \sin(2\pi t/\tau)$, with $T = 20\tau$, $\tau = 1$, $\Delta t = 0.01\tau$ and $N' = T/\Delta t$, for fatigue estimation. The red regions in Fig. 9 indicate elements that utilize the domain extension approach, i.e., $x_e = \epsilon$, while the regions under the load and around the bolts indicate elements that are not included in optimization.

The fatigue constrained problem (TO) is solved for two cases. In the first case, the fatigue model is fully integrated to $t_N = 20\tau$ with $\bar{D} = 1E-5$, while in the second we use Algorithm 1 to identify the steady-state condition that exists after $t_A = 14\tau$. Thus the fatigue model is fully integrated until t_A with extrapolation to $t_N = 20E5\tau$. The fatigue bound is taken as $\bar{D} = 0.9$. The compliance bound for both cases is taken as $\bar{C} = 3.8 \text{ Nmm}$.

The optimized result of the 3D bracket for the first case after solving (TO) problem is shown in Fig. 10(b). The computational time required to solve this problem after 500 iterations is around 10 h. For comparison, Fig. 10(a) provides the optimization result for the mass minimization problem without fatigue constraint. We notice that there is a considerable change in the profile of the optimized model, Fig. 10(b), to account for fatigue constraint when compared to Fig. 10(a).

In the second case, (TO) is solved with extrapolation. Here, we fully integrate the fatigue model until t_A with extrapolation to $t_N = 20E5\tau$. The optimized model is shown in Fig. 10(c). The computational time required to solve this problem after 500 iterations is around 5.5 h.

7. Conclusion

An acceleration technique was proposed to treat continuous-time constrained TO fatigue problems, (Suresh et al., 2020). Through this technique we can solve TO problems for unlimited load histories comprising sequence repetitions.

Fatigue sensitivities were derived by the adjoint method. However, the computational effort is quite high (around $N \times n^2$), and is mainly due to the solution of the adjoint variables. Hence, a technique was proposed, where we utilized extrapolation for the continuous-time model, based on the fact that the HCF model exhibits a steady-state condition for all forms periodic, proportional and most non-proportional loads. Along with this technique, we further speed up the sensitivity analysis by identifying and eliminating some time steps from the analysis.

Considering 7050-T7451 aluminum alloy, several numerical examples were given. An L-shaped beam subject to not only constant-amplitude cycles but also a repeated load spectrum, proportional load histories are presented. Additionally, we present the same L-shaped beam subject to a biaxial, non-proportional load history. For these load histories, through continuous-time approach, the HCF model attains a steady-state condition and through extrapolation, we solved the (TO) problem for a long load history. We notice there are small changes in the optimized designs due to the extrapolation technique, but no significant change in mass. Finally, we also presented a 3D bracket

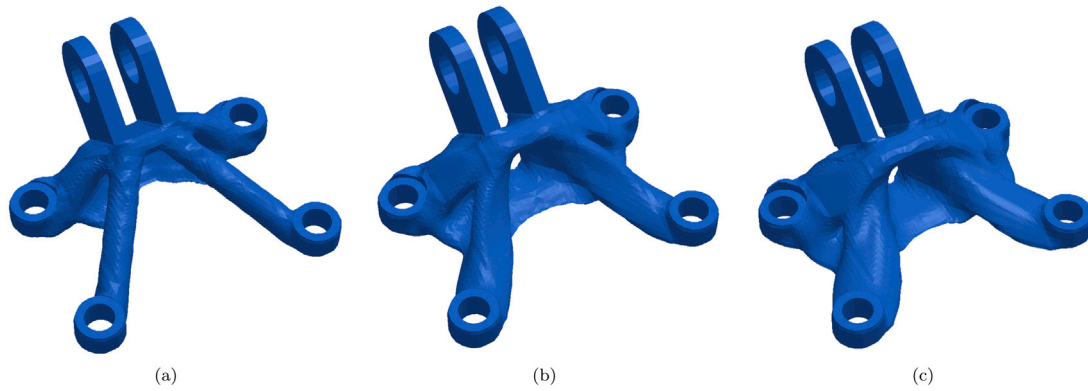


Fig. 10. Optimized model (iso-surface when $\rho = 0.5$) of the 3D bracket: (a) Without fatigue constraint, where the obtained optimized mass is 0.078 kg; (b) With fatigue constraint when fully integrated to $t_N = 20r$, and the obtained optimized mass is 0.103 kg; (c) With fatigue constraint when extrapolation is used (extrapolated to $t_N = 20E5r$), and the obtained optimized mass is 0.125 kg.

with periodic load history, thus demonstrating the capability to handle industrial-scale problems subjected to a long load history.

In this research we present acceleration techniques only for isotropic materials. However it is also possible to treat transversely isotropic materials (Suresh et al., 2021).

Declaration of competing interest

The authors declare the following financial interests/personal relationships which may be considered as potential competing interests: Anders Klarbring reports financial support was provided by Sweden's Innovation Agency.

Data availability

Data will be made available on request.

Acknowledgements

The work was performed within the Centre for Additive Manufacturing-Metal (CAM²) financed by Sweden's Innovation Agency under grant agreement No 2016-05175.

References

- Bendsoe, M.P., Sigmund, O., 2004. *Topology optimization: theory, methods, and applications*. Springer Science & Business Media.
- Brighenti, R., Carpinteri, A., Vantadori, S., 2012. Fatigue life assessment under a complex multiaxial load history: an approach based on damage mechanics. *Fatigue Fract. Eng. Mater. Struct.* 35, 141–153.
- Bruggi, M., 2008. On an alternative approach to stress constraints relaxation in topology optimization. *Struct. Multidiscip. Optim.* 36, 125–141.
- Bruns, T.E., Tortorelli, D.A., 2001. Topology optimization of non-linear elastic structures and compliant mechanisms. *Comput. Methods Appl. Mech. Engrg.* 190, 3443–3459.
- Christensen, P., Klarbring, A., 2009. *An Introduction to Structural Optimization*, Solid Mechanics and its Applications. Springer Netherlands.
- Clausen, A., Andreassen, E., 2017. On filter boundary conditions in topology optimization. *Struct. Multidiscip. Optim.* 56, 1147–1155.
- Collet, M., Bruggi, M., Duysinx, P., 2017. Topology optimization for minimum weight with compliance and simplified nominal stress constraints for fatigue resistance. *Struct. Multidiscip. Optim.* 55, 839–855.
- Duysinx, P., Sigmund, O., 1998. New developments in handling stress constraints in optimal material distribution. <http://dx.doi.org/10.2514/6.1998-4906>, <https://arc.aiaa.org/doi/abs/10.2514/6.1998-4906> <http://arxiv.org/abs/https://arc.aiaa.org/doi/pdf/10.2514/6.1998-4906>.
- Holmberg, E., Torstenfelt, B., Klarbring, A., 2013. Stress constrained topology optimization. *Struct. Multidiscip. Optim.* 48, 33–47.
- Holmberg, E., Torstenfelt, B., Klarbring, A., 2014. Fatigue constrained topology optimization. *Struct. Multidiscip. Optim.* 50, 207–219.
- Holopainen, S., Kouhia, R., Saksala, T., 2016. Continuum approach for modelling transversely isotropic high-cycle fatigue. *Eur. J. Mech. A Solids* 60, 183–195.
- Jeong, S.H., Lee, J.W., Yoon, G.H., Choi, D.H., 2018. Topology optimization considering the fatigue constraint of variable amplitude load based on the equivalent static load approach. *Appl. Math. Model.* 56, 626–647.
- Kennedy, G.J., Hicken, J.E., 2015. Improved constraint-aggregation methods. *Comput. Methods Appl. Mech. Engrg.* 289, 332–354.
- Lindström, S.B., 2020. Continuous-time, high-cycle fatigue model for nonproportional stress with validation for 7075-t6 aluminum alloy. *Int. J. Fatigue* 140, 105839.
- Lindström, S.B., Thore, C.-J., Suresh, S., Klarbring, A., 2020. Continuous-time, high - cycle fatigue model: Validity range and computational acceleration for cyclic stress. *Int. J. Fatigue* 136, 105582.
- Oest, J., Lund, E., 2017. Topology optimization with finite-life fatigue constraints. *Struct. Multidiscip. Optim.* 56, 1045–1059.
- Ottosen, N.S., Ristinmaa, M., Kouhia, R., 2018. Enhanced multiaxial fatigue criterion that considers stress gradient effects. *Int. J. Fatigue* 116, 128–139.
- Ottosen, N.S., Stenström, R., Ristinmaa, M., 2008. Continuum approach to high-cycle fatigue modeling. *Int. J. Fatigue* 30, 996–1006.
- Suresh, S., Lindström, S., Thore, C.-J., Klarbring, A., 2021. Topology optimization for transversely isotropic materials with high-cycle fatigue as a constraint. *Struct. Multidiscip. Optim.* 63.
- Suresh, S., Lindström, S., Thore, C.-J., Torstenfelt, B., Klarbring, A., 2020. Topology optimization using a continuous-time high-cycle fatigue model. *Struct. Multidiscip. Optim.* 61, 1011–1025.
- Svanberg, K., 1987. The method of moving asymptotes—a new method for structural optimization. *Internat. J. Numer. Methods Engrg.* 24, 359–373.
- Torstenfelt, B., 2012. *The TRINITAS project*. https://www.solid.iei.liu.se/Offered_services/Trinitas, https://www.solid.iei.liu.se/Offered_services/Trinitas.
- Wang, W., Clausen, P.M., Bletzinger, K.-U., 2017. Efficient adjoint sensitivity analysis of isotropic hardening elastoplasticity via load steps reduction approximation. *Comput. Methods Appl. Mech. Engrg.* 325, 612–644.
- Yang, R.-J., Chen, C.-J., 1996. Stress-based topology optimization. *Struct. Multidiscip. Optim.* 12, 98–105.
- Zhang, S., Le, C., Gain, A.L., Norato, J.A., 2019. Fatigue-based topology optimization with non-proportional loads. *Comput. Methods Appl. Mech. Engrg.* 345, 805–825.